



Full Text View

[Volume 29, Issue 5 \(May 1999\)](#)

Journal of Physical Oceanography

Article: pp. 837–864 | [Abstract](#) | [PDF \(883K\)](#)

Instability Dynamics of a Subtropical Jet and Applications to the Azores Front Current System: Eddy-Driven Mean Flow

Mário L. G. R. Alves

Department of Oceanography and Fisheries, Azores University, Azores, Portugal

A. Colin de Verdière

Laboratoire de Physique des Océans, Université de Bretagne Occidentale, Brest, France

(Manuscript received August 19, 1997, in final form April 22, 1998)

DOI: 10.1175/1520-0485(1999)029<0837:IDOASJ>2.0.CO;2

ABSTRACT

The Azores front is associated with an eastward flowing subtropical jet, which coincides with the northern edge of the North Atlantic subtropical gyre and forms a southern branch of the Gulf Stream. An intensive study of the eddy-driven mean flow induced by the nonlinear instability of the jet has been conducted. Using a primitive equation numerical model initialized with the summer hydrological fields typical of the Azores front, the authors show that

1. the mesoscale patterns that appear after a few months are largely determined by baroclinic instability processes.
2. the jet and its associated mesoscale turbulence have a strong meridional asymmetry due to the strongly sloping thermocline. In general, an anticyclonic meander, which grows and deforms northwestward, generates a pinched-off anticyclone while a cyclonic meander, which grows and deforms southwestward, degenerates in a thin filamental structure that will dissipate before any cyclone can be pinched off. The authors propose a mechanism that relates this asymmetry of the turbulent fields to the mean meridional gradient of Ertel potential vorticity.
3. the rectification of the meridionally asymmetric mesoscale turbulent eddies is able to create a westward flowing countercurrent on the northern flank of the main jet. The Eliassen–Palm flux vector divergence or, equivalently, the turbulent transport of Ertel potential vorticity perturbation drives the countercurrent in the upper layers, while the

Table of Contents:

- [Introduction](#)
- [Climatology of the AzC](#)
- [Model description and](#)
- [The mesoscale turbulent](#)
- [Energetics and dominant](#)
- [Zonal mean flow dynamics](#)
- [Conclusions](#)
- [REFERENCES](#)
- [TABLES](#)
- [FIGURES](#)

Options:

- [Create Reference](#)
- [Email this Article](#)
- [Add to MyArchive](#)
- [Search AMS Glossary](#)

Search CrossRef for:

- [Articles Citing This Article](#)

Search Google Scholar for:

- [Mário L. G. R. Alves](#)
- [A. Colin de Verdière](#)

Coriolis force acting over the ageostrophic meridional circulation is responsible at lower levels. This ageostrophic meridional circulation is dipolar, with an upwelling below the jet axis and downwellings on either sides. The dipole is forced by the particular structure of the eddy transport of zonal momentum associated with meridional asymmetry. It is an important communication link between the surface and deeper ocean layers in a frontal area. These results are in good agreement with observational data from the Azores Front system and are probably relevant to other zonal jets that lie on the poleward sides of subtropical gyres.

1. Introduction

The instability processes at oceanic subtropical fronts is of fundamental importance in the maintenance of the time-averaged oceanic circulation as well as in the exchange of properties across the front, exchanges that also have strong biological implications. Such semipermanent fronts as the Azores Front to be studied herein appear as abrupt boundaries between warm central waters and colder mode waters that invalidate the concept of an interior semipermanent circulation on a scale large compared to the Rossby radius of deformation. Situated on the poleward boundaries of subtropical gyres, the narrowness and vertical shear of these eastward jets make them prone to instabilities, especially baroclinic, with the subsequent development of an equilibrium between an energetic time-dependent eddy field and the mean jet.

The basic state of the jets can be observed by making use of climatological and synoptic hydrological data, and it is then appropriate to search for the properties of the equilibrium by hydrodynamical modeling of the eddy generation process. Indeed, [Gill et al. \(1974\)](#) suggested through a linear stability analysis that baroclinic instability was a process likely to be operative to explain the presence of midocean eddies that were being discovered at that time. As eddy-resolving numerical models appeared, the same instability processes were shown at work in the eddy-rich region of western boundary current extensions in quasigeostrophic (QG) wind-driven circulation models, ([Haidvogel and Holland 1978](#)). Simpler unforced zonal jets were analyzed by [Rhines \(1977\)](#) and [Ikeda \(1981\)](#), who showed the processes of tendency to barotropy and eddy detachment in two-layer QG models. Later, [Beckman \(1988\)](#), [De Mey \(1994\)](#), and [Feliks and Ghil \(1996\)](#) initialized narrow subtropical jets emphasizing the mixed nature (barotropic–baroclinic) of the instability. However, because subtropical jets mark a boundary between water types, the isopycnals have large vertical excursions that limit the usefulness of quasigeostrophic results. Many studies such as [Samelson and Chapman \(1995\)](#) and [Spall \(1995\)](#) have returned to the use of primitive equation models (PE) to study the frontogenesis of shallow mixed layer jets. Apparently, only the work of [Kielmann and Käse \(1987\)](#) addressed specifically the modeling of thicker subtropical jets such as the Azores, concentrating on the initial phase evolution of the instability cycle. That study will be pursued here for a full nonlinear instability cycle (growth and decay) and an attempt will be made to explain the interaction of eddies and mean flows observed in the Azores front–current system (AzC). Crucial to the pattern of the simulated mesoscale turbulence is the presence of the steeply sloping mean thermocline: this will cause an asymmetry between cyclones and anticyclones absent from QG simulations that appear relevant to the observations. Because the stability properties of upper-ocean currents are very sensitive to the shape of the velocity profiles (Gill et al. 1974), it is important to initialize the models with mean profiles as realistic as possible and let instability processes provide the characteristics of the unstable wave field. For longer time integration, many other parameters of the model (subgrid-scale friction and diffusivity, climatological forcing of the mean flow) must be chosen to generate a realistic eddy field. It was decided to tune these unknown coefficients to reproduce the observed bulk eddy energy levels of a given region, restricting thereby the analysis to that of the local interaction between eddies and mean flow, the external energy sources, that is, climatological forcing, that maintain the jet being imposed a priori. Unavoidably, this strategy requires a focus on a specific region. Because of its importance in the North Atlantic circulation, the region of the Azores front current appears to be a good starting point and we feel that other subtropical jet regions can be compared usefully at some later stage with the present results.

Previous work refers to the Azores Current as quasipermanent throughout the year, with eastward transport of some 10 Sv ($Sv \equiv 10^6 \text{ m}^3 \text{ s}^{-1}$) southeast of the Azores Islands and identified as almost zonal along the northern/northeastern flank of the North Atlantic subtropical gyre, between 33° and 35°N ([Klein and Siedler 1989](#); [Schmitz and McCartney 1993](#); [Maillard and Käse 1989](#); [Stramma and Siedler 1988](#); [Müller and Siedler 1992](#); [Alves et al. 1994](#)). A few climatological studies present it as a shallow baroclinic feature, no deeper than 1000 m ([Klein and Siedler 1989](#); [Ollitrault 1995](#); [Bigg 1990](#)).

Surface mean speed value is situated around 30 cm s⁻¹ decreasing to very small values at 700 m ([Ollitrault 1995](#)). Many of the previously mentioned works also refer to the jet as a source of high mesoscale variability. Meanders of wavelength 200–300 km and some 150 km of amplitude have been reported by [Kielmann and Käse \(1987\)](#), while observations of energetic time periods of 20 to 120 days have been presented by [Maillard and Käse \(1989\)](#). Using two years of Geosat altimetric data, [Le Traon and De Mey \(1994\)](#) observed a north–south asymmetry with greater variability on the northern flank of the jet axis. This same asymmetric pattern is also clearly visible in the satellite infrared picture of surface temperature presented by [Kielmann and Käse \(1987\)](#) for the AzC system. All these observations point out the need to model such subtropical jets with more general PE models to which the following questions may be addressed:

Are the observed characteristic characteristics of the eddies well captured in the initial phase of the instability? On the nonlinear equilibration timescale? What is the nature of the wave–eddy–mean flow dynamical interaction on these same two timescales?

In [section 2](#) a climatological study of the Azores front is made using about 50 years of National Oceanic Data Center (NODC) hydrological data for the area. This is followed by an intensive study of mesoscale instability processes, initializing [Haidvogel et al. \(1991\)](#)'s primitive equations model with a particular summer hydrological synoptic field ([sections 3–4](#)). Energetics and mean flow rectification are explored in [section 5–6](#) using the transformed Eulerian mean (TEM) analysis pioneered by [Edmond et al. \(1980\)](#) in an atmospheric context.

2. Climatology of the AzC region

A good instability analysis requires initialization of the temperature/salinity fields at high resolution, information that is not readily available in the case of the Azores front. Often synoptic surveys reveal a meandering jet situation from which it is difficult to extract an initial jet unperturbed by unstable eddies. In order to prepare this initialization, it was decided first to reconstruct a climatology of the area with as little smoothing as possible and then to use a synoptic situation that would be close to the climatology but would produce more realistic slopes of the initial front. An objective analysis of NODC hydrological (temperature and salinity) data for the period 1945–91, with $1^\circ \times 1^\circ$ spatial resolution was performed for each season in the box $20^\circ\text{--}50^\circ\text{N}$, $0^\circ\text{--}50^\circ\text{W}$. A method of analysis with less smoothing and 10 more years of data make this local study a significant improvement over the [Levitus \(1982\)](#) climatology of the region, which does not resolve wavelengths shorter than about 500 km (cf. his [Fig. 11](#)). From the resulting optimal temperature and salinity fields, the density field and geostrophic velocities from the thermal wind equation can be inferred:

$$\begin{aligned} \mathbf{v}_g(x, y, z) \\ = \frac{g}{\rho_0 f} \int_{-H}^z \left[\frac{\partial}{\partial y} \rho(x, y, z) \mathbf{e}_1 - \frac{\partial}{\partial x} \rho(x, y, z) \mathbf{e}_2 \right] dz, \quad (1) \end{aligned}$$

where \mathbf{e}_1 and \mathbf{e}_2 are unit vectors directed, respectively, eastward and northward.

Using a reference level at 2000 m, the Azores Current appears in [Fig. 1](#) to be an almost zonal eastward flowing current, extending meridionally over 5° of latitude and reaching clearly the eastern boundary in the region of the Gulf of Cadiz. Large-scale maximum surface mean speeds are between 5 and 10 cm s^{-1} . Since the Azores Current is almost zonal between 25° and 35°W , the zonal mean is shown for each season and for the annual average in [Fig. 2](#). The eastward jet is centered around 34°N , with a maximum intensity at the surface. It exists throughout the year and, in general, does not penetrate deeper than 1000 m, except in spring when a maximum depth of 1500 m is reached. At the southern limit of each section, part of the westward flowing Cape Verde Current can be seen, while only the southernmost signature of the North Atlantic Current is observed flowing eastward at the northern limit of the represented area. Note the subsurface (maximum intensity at depth between 200 and 500 m) westward flowing Azores Countercurrent (AzCC) on the northern flank of the Azores Current, which is maximum in spring ([Alves and Colin de Verdière 1996](#)). [Klein and Siedler \(1989\)](#) and [Stramma and Isemer \(1988\)](#) found an AzCC signal between 200 and 800 m, and it was first explicitly mentioned by [Onken \(1993\)](#). However, neither a seasonal analysis was performed nor an explanation for its subsurface intensification given. More recently hydrography and ERS-1 altimetry combined by [Cromwell et al. \(1996\)](#) to reveal a rather persistent, westward surface current north of the main jet that was assumed to be a retroreflection of the main jet. [Table 1](#) shows the Azores Current and Countercurrent seasonal transports that we have estimated with errors, respectively, of 1 and 0.2 Sv. These errors come from the variation of the reference level from 1500 to 2500 m. Annual mean values of about 13 and 2 Sv are obtained, respectively, for the mean jet and its countercurrent. In both cases zonal mean transports increase suddenly from winter to spring and then decay more slowly during the rest of the year. Although the existence of the main jet is assumed a priori in the present study, a central result that we demonstrate in what follows is that the countercurrent is driven by eddies and meander deformation, themselves generated by the instability of the main jet, in contrast with the wind-forcing mechanism proposed by [Onken \(1993\)](#).

3. Model description and basic instabilities

a. The model

Simulations of the instability processes of the main jet are carried out with the PE SPEM code (in its spectral 3.9 version) described by [Haidvogel et al. \(1991\)](#), which solves equations for the ocean velocity (u, \mathbf{v}, w) , potential temperature θ and salinity S :

$$\begin{aligned} \frac{\partial u}{\partial t} + (\mathbf{v} \cdot \nabla)u - fv &= -\frac{\partial \phi}{\partial x} + k_H \nabla_H^4 u + \frac{\partial}{\partial z} \left(k_v \frac{\partial u}{\partial z} \right) \\ &\quad - \left(\frac{(u - u_{\text{clm}})}{T_d} \right) \end{aligned} \quad (2)$$

$$\begin{aligned} \frac{\partial v}{\partial t} + (\mathbf{v} \cdot \nabla)v + fu &= -\frac{\partial \phi}{\partial y} + k_H \nabla_H^4 v + \frac{\partial}{\partial z} \left(k_v \frac{\partial v}{\partial z} \right) \\ &\quad - \left(\frac{(v - v_{\text{clm}})}{T_d} \right) \end{aligned} \quad (3)$$

$$\frac{\partial \phi}{\partial z} = -\frac{\rho}{\rho_0} g \quad (4)$$

$$\nabla \cdot \mathbf{v} = \frac{\partial u}{\partial x} + \frac{\partial v}{\partial y} + \frac{\partial w}{\partial z} = 0 \quad (5)$$

$$\begin{aligned} \frac{\partial \theta}{\partial t} + (\mathbf{v} \cdot \nabla)\theta &= k_H^\theta \nabla_H^4 \theta + \frac{\partial}{\partial z} \left(k_v^\theta \frac{\partial \theta}{\partial z} \right) \\ &\quad - \left(\frac{(\theta - \theta_{\text{clm}})}{T_d} \right) \end{aligned} \quad (6)$$

$$\begin{aligned} \frac{\partial S}{\partial t} + (\mathbf{v} \cdot \nabla)S &= k_H^S \nabla_H^4 S + \frac{\partial}{\partial z} \left(k_v^S \frac{\partial S}{\partial z} \right) \\ &\quad - \left(\frac{(S - S_{\text{clm}})}{T_d} \right) \end{aligned} \quad (7)$$

$$\rho = \rho(\theta, S, p). \quad (8)$$

In order to maintain the structure of the jet (not represented by the regional model), a term of the form $-(\chi - \chi_{\text{clm}})/T_d$ is added to the horizontal momentum and potential temperature and salinity conservation equations in the case of long-term integrations (χ may be any of the fields u , v , θ , or S). Such a term represents the effects of the general circulation not represented in the regional model: a persistent restoring of the state of the model toward the climatology occurs on a timescale T_d . Several T_d values (ranging from a few days to several years) have been used, showing that the model spectral signatures remain similar. However, in order to have a fixed T_d value for the base run we decided to choose a timescale that allowed a realistic level of turbulent kinetic energy of the area. Lagrangian subsurface floats deployed during the Topogulf experiment (Ollitrault 1995), allowed accurate mapping of the eddy kinetic energy at 700 m. Although this is the lower base of the Azores Current, the float data reveals a tongue of higher eddy kinetic energy elongated along the path of the mean jet. The value of $T_d = 100$ days yielded model values of eddy kinetic energy close to the observed ones.

The geometry chosen for the model simulations is that of a zonally periodic beta-plane channel 480 km long, 640 km wide, and 2000 m deep. Horizontal resolution of 10 km and 16 vertical levels were used. The zonal length, allowed to fit two unstable waves, was compatible with the computer resources given the relatively high resolution desired. The channel is relatively wide because our objective is to study an open ocean jet, so the influence of the lateral boundaries must be

minimized. To do so, we found it necessary to damp the internal gravity waves of near-inertial frequency that the initial adjustment invariably generates. These waves are produced in the vicinity of the jet and propagate at group velocities of order 1.5 m s^{-1} toward the north and south boundaries where they reflect back in the interior. To suppress these reflections a sponge layer 100 km wide was introduced near the northern and southern boundaries whose effect is to restore the model state toward the initial state with a very small time constant of 8 h. No flux velocity boundary conditions are prescribed at the surface and bottom as the rigid-lid approximation is used and there is no topography. The shallow depth that was used deserves some comments. After initial tests we found that vertical resolution was really the important factor and that, given the same vertical resolution, the characteristics of the instability were essentially unchanged for 2000-m or 4000-m depth, a likely reason being the surface-intensified nature of the jet, so we chose the former to reduce computation costs. There are no external forcings such as wind stress or buoyancy flux. To free the major nonlinear interactions from the influence of friction, a biharmonic operator was chosen with values of $10^{10} \text{ m}^4 \text{ s}^{-1}$ and $10^9 \text{ m}^4 \text{ s}^{-1}$, respectively, for the momentum and tracer fields.

b. Basic-state initialization

It is our intention to describe and explain the subtropical character of mesoscale patterns generated by the instability of the main jet, as well as to explore their consequences. We initialize the model tracer fields from observations but avoid, deliberately, the presence of Mediterranean Water (which is present below 800 m) and, above all, the presence of the countercurrent since it is our conjecture that this particular feature is a by product of local nonlinear interactions between unstable waves and the main jet. Model initialization is achieved through the use of a prototype mean summer synoptic situation observed during the CODFRA/92¹ cruise, which took place during the summer of 1992 (Alves et al. 1993). At the time, the eastward flowing jet found south of the Azores Islands was centered around 34°N and appeared little disturbed by the mesoscale turbulence, a unique situation to initialize the model with realistic speeds and frontal widths. To obtain an analytic expression for the tracer fields, we first determined the summer meridional temperature and salinity differences across the front as a function of pressure (Fig. 3). Note that the differences are maximum in the main thermocline for both T and S and disappear for temperature at the surface but remain for salinity (although weaker). A least square fit of these property differences has been carried out with the function

$$\Delta\chi(z) = d_0 z \exp\left(-\frac{z}{g_0}\right), \quad (9)$$

where $\chi \equiv T, S$ and d_0, g_0 are the best-fit parameters. Similarly, the north and south temperature and salinity vertical profiles have been fitted to a function of the type

$$\chi(y=0, z) = a_0 \exp(b_0 z) + \chi_0, \quad (10)$$

where a_0, b_0 are the least squares best-fit parameters and χ_0 is a constant parameter.

With the help of these two fits, the $\chi(y, z)$ property field is chosen to be represented in the meridional depth plane as

$$\chi(y, z) = \chi(y=0, z) + \left[\tanh\left(\frac{cy}{L} - \frac{c}{2}\right) + 1 \right] \frac{\Delta\chi(z)}{2}, \quad (11)$$

with $0 \leq y \leq 640 \text{ km}$, $-2000 \text{ m} \leq z \leq 0 \text{ m}$, and where $\chi(y=0, z)$ is given by (10), $\Delta\chi(z)$ by (9). A hyperbolic tangent profile in the meridional direction is adequate, with c a parameter adjusted by a final least square fit to the observed meridional profile. After determination of the observed and reconstructed geostrophic vertical shears, c is chosen as that value that minimizes (12) the mean square difference between observed and reconstructed geostrophic velocities:

$$\Psi^2 = \frac{1}{\sigma^2} \sum_{i=1}^n (u_{gi}^{\text{obs}} - u_{gi}^{\text{mod}})^2. \quad (12)$$

With the result $c = 24.5$, these best fits (Fig. 4) show good agreement between the synoptic situation and the analytic representation of the jet whose net transport is now 8.5 Sv. The model run is thus initialized with the described T and S fields and with the associated geostrophic current field. A flat-bottom isopycnal surface allows us to use a 2000-m level of no motion to integrate the thermal wind relation and obtain a net transport of 8.5 Sv. The external streamfunction is thus

calculated by the model for this initial geostrophic field. The total transport of 8.5 Sv will remain invariant throughout the model run, although the mean meridional current structure is free to change in time.

c. QG linear instability analysis

The initial fields distribution represents the basic state in the sense of instability theory, and it is important to know if the basic state is unstable to barotropic and/or baroclinic instability. We first consider the instability criterion appropriate to each type of instability known under QG theory (Pedlosky 1987). The Charney–Stern necessary condition for linear instability of a zonal jet varying in the meridional and vertical direction is that, at least, one of the meridional gradients

$$\left. \frac{\partial Q_B}{\partial y} \right|_{\text{interior}}, \quad \left. \frac{\partial \rho_B}{\partial y} \right|_{\text{bottom}}, \quad - \left. \frac{\partial \rho_B}{\partial y} \right|_{\text{top}} \quad (13)$$

must change sign somewhere within the domain, where


$$\left. \frac{\partial Q_B}{\partial y} \right|_{\text{interior}} = \beta - \left. \frac{\partial^2 U_B}{\partial y^2} \right|_{\text{interior}} - f_0^2 \left. \frac{\partial}{\partial z} \left(\frac{1}{N_B^2} \frac{\partial U_B}{\partial z} \right) \right|_{\text{interior}} \quad (14)$$

is the meridional gradient of QG potential vorticity Q_B , ρ_B the density, $U_B(y, z)$ the zonal geostrophic current, and $N_B(y, z)$ the buoyancy frequency (subscript B stands for basic state). In particular, if the velocity varies only in the vertical direction (baroclinic case), then (14) becomes

$$\left. \frac{\partial Q_B}{\partial y} \right|_{\text{interior}} = \beta - f_0^2 \left. \frac{\partial}{\partial z} \left(\frac{1}{N_B^2} \frac{\partial U_B}{\partial z} \right) \right|_{\text{interior}}, \quad (15)$$

while if the velocity varies only in the meridional direction (barotropic case), then

$$\left. \frac{\partial Q_B}{\partial y} \right|_{\text{interior}} = \beta - \left. \frac{\partial^2 U_B}{\partial y^2} \right|_{\text{interior}}. \quad (16)$$

These two quantities are illustrated in [Fig. 5a and 5b](#) , respectively, and both figures show that $\partial Q_B / \partial y$ changes sign inside the domain, for both baroclinic and for barotropic reasons. The stretching term enhances the β effect in the first 250 m because of the slope of the thermocline, while $\partial Q_B / \partial y$, becoming negative down to about 1000 m, opposes the planetary gradient. Similarly, the horizontal curvature of the zonal flow is strong enough to overcome β and allow a zero PV gradient. For future reference it is useful to use the Phillips two-layer model to estimate the most unstable wavelength in the baroclinic case. With a mean vertical shear of 30 cm s^{-1} , a reduced gravity $g' = 0.012 \text{ m s}^{-2}$ and an upper layer $H = 800 \text{ m}$, a maximum growth rate is obtained at a wavelength $2\pi C/f$ ($=230 \text{ km}$), where C/f ($=37 \text{ km}$) is the internal Rossby radius [with $C = (gH\Delta\rho/\rho_0)^{1/2}$].

d. Primitive equation instability analysis

The best way to obtain the preferred scales of instability and to identify the key energy conversions in these complex mixed cases is to use the PE model in a free decay simulation (without restoring to climatology), itself properly initialized. This has to be PE because of the large excursions of the isopycnals observed. The previously determined best-fit distributions being used for the initialization, an initial perturbation is needed to trigger the instability. In order to detect the fastest growing wave, care must be taken that the initial perturbation does not favor a particular scale by itself. We have chosen to perturb the meridional velocity with a surface intensified structure and a Gaussian shape in the meridional direction, while a white noise spectrum of random waves is used in the zonal direction:

$$v'(x, y, z) = v_f \exp \left[- \left(\frac{y}{L_y} - \frac{1}{2} \right)^2 \right] \exp \left(- \frac{z}{z_{\text{inf}}} \right) \times \sum_{m=1}^{L_x/2\Delta x} \sin \left(\frac{2\pi}{L_x} m \Delta x + \varphi_m(x) \right), \quad (17)$$



where $v_f = 10^{-4} \text{ m s}^{-1}$ is a small maximum meridional speed amplitude, L_x (L_y) is the zonal (meridional) channel length, and φ_m is a random initial phase. According to (17) the initial perturbation will be surface intensified and decrease to zero in both north and south boundaries. Since our channel is zonally periodic, we can only have a finite integer number of unstable wavelengths inside the domain whose maximum is $m = L_x/(2\Delta x)$, which, for example with $L_x = 480 \text{ km}$ and $\Delta x = 10 \text{ km}$ gives $m = 24$. So, the most unstable wavelength will naturally become one of these. It is problematic, however, that the low wavenumber range has too little resolution. To have sufficient resolution at the low-wavenumber end and estimate correctly the fastest growing wavelength, a long channel length of 2560 km has been used for these nonlinear unforced instability calculations. Once the model is run with such a perturbed initial state, the most unstable waves are obtained by Fourier analyzing the meridional velocity in the zonal direction. This readily allows us to find out how the amplitude of a given zonal wavelength evolves with time (Fig. 6). Significant amplitudes appears after day 50. Until day 90, the 160-km wavelength is preferred, while later on the maximum grows to a 240-km wavelength through a nonlinear interaction process between meanders (as explained later). The 160-km wavelength, on the other hand, is probably associated with linear instability, in which case is significantly smaller than what is predicted by the two-layer model. Between wavelengths 100 and 200 km, the spectral amplitudes vacillate with a period of around 50 days. This corresponds to spatial structures that are quickly reducing their sizes (e.g., the most significant feature, with 240-km length present at day 150, is decreasing to 100 km in about 10 days).

The sensitivity of these favored scales to the horizontal and vertical resolutions (as well as to the total channel depth) has been tested. Increasing horizontal resolution did not reveal significant changes. Vertical resolution is more sensitive. Using 9 vertical levels instead of 16 causes an increase from 5% to 10% in the most unstable wavelength. Increasing the number of levels to 26 did not change the result. So we may be reasonably confident that the 160-km (240 km) wavelengths are good determinations of the most unstable waves of the Azores jet at respectively small (large) amplitudes.

4. The mesoscale turbulent field

We now proceed to describe the turbulence under forced conditions in the short channel case when restoring to initial conditions is included. In such cases it takes about 100 days for the mesoscale turbulence kinetic energy to equilibrate. The developed surface mesoscale patterns reveal pinched-off anticyclonic eddies along the northwestern flank (Fig. 7a) and northeastern flank (Fig. 7b). The nonlinear interaction of the latter with a nearby downstream propagating jet meander generates a noncircular anticyclonic eddy around day 170 (Fig. 7c). The middepth ($z = 1050 \text{ m}$) current patterns (Figs. 8a–c) reveal the formation of a coherent zonal Azores Countercurrent flow that extends down to the bottom of the domain. We will show in section 6 that the surface AzCC signal (above about 250 m) is due to the quasicohent anticyclones, while at depth the meander circulation is responsible for the zonal westward flow. Analyzing an entire period of 4 years, we note a clear and persistent tendency for enhanced anticyclonic activity. This is an important manifestation of the meridional asymmetry of the jet, with anticyclones forming and pinching off to the north of the jet axis, while no cyclones can survive long enough to the south and only cyclonic filaments are left behind. The baroclinic structure of these mesoscale features can be revealed through a meridional cross section of zonal velocities. While the main jet is intensified above 1000 m, the anticyclonic features, although surface intensified, have a signature at depth. The southern cyclonic features, on the other hand, are shallower and do not reach the bottom (Fig. 9).



The vertical velocity field w is calculated diagnostically after integration of the continuity equation (5). The spatial position of the upwelling and downwelling centers associated with the nonlinear unstable wave meanders generated by the model are in good agreement with previous results of Kielmann and Käse (1987), Onken (1992), and Wang (1993). That is, given an anticyclonic meander of the unstable wave, downwelling (upwelling) forms respectively along the southeastward and northeastward flowing branch (Fig. 10). Representing the time evolution of the vertical velocity field in an $x-t$ characteristic diagram, the phase propagation of the unstable features can be deduced. Doing this for the jet axis line ($y = 320 \text{ km}$), we can see that between days 50 and 90, the dominant unstable wave, which has a wavelength of 160 km, propagates quickly eastward at a phase speed of $c_f \cong 5.3 \text{ km day}^{-1}$ (Fig. 11). From days 90 to 120, a nonlinear interaction between the deforming meanders causes the merging of two meanders, producing an increase (240 km) of the most unstable wavelength. This can also be noticed in the time-varying wavenumber energy spectra (Fig. 6) between days 90 and 120, where the 240-km peak appears to be enhanced by the shorter wavelengths with no signal coming from

the longer ones. Simultaneously, the eastward propagation slows to $c_{II} \approx 2.4 \text{ km day}^{-1}$. Note, however, the superposition of faster eastward propagating events at a speed of $c_{III} \approx 5.0 \text{ km day}^{-1}$. A close inspection of each dipole of up/downwelling intensity maximum in an anticyclonic meander reveals that, at a given instant, one is propagating faster than the other in a way compatible with a tendency for the up/down dipole to rotate in the cyclonic sense. This cyclonic rotation is associated with a northwestward deformation of the anticyclonic meander. [Figure 12](#)  represents a sketch of this process, which also occurs south of the jet. Similar $x-t$ characteristic diagrams for two symmetric positions relatively to the jet axis ($y = 220 \text{ km}$ and $y = 420 \text{ km}$) reveal similar propagation patterns (Alves 1996). However, for the northern one ($y = 420 \text{ km}$) we can also identify westward propagating signals at a phase speed of 2 km day^{-1} . This is the result of the propagation of anticyclonic eddies and marks again the meridional asymmetry of the turbulent eddy field. We note further that there is about a 40-day lag between the development of an intense vertical movement at the channel axis (starting around day 40 in [Fig. 11](#) ) and its arrival at the southern and northern sections 100 km away. This yields a displacement rate of about 2.5 km day^{-1} .


The Ertel potential vorticity (EPV) appropriate to hydrostatic PE model formulations can be written as

$$q = \frac{1}{\rho} \left[-\frac{\partial v}{\partial z} \frac{\partial \rho}{\partial x} + \frac{\partial u}{\partial z} \frac{\partial \rho}{\partial y} + (f + \xi) \frac{\partial \rho}{\partial z} \right], \quad (18)$$

where ξ is the vertical component of relative vorticity.

The initial distribution of q ([Fig. 13](#) ) is already meridionally asymmetric with extremal values (minimum) concentrated in a shallow layer on the northern flank of the jet. However, q contours are perfectly zonal at the beginning. In the turbulent regime, during which most of the eddy pinch-off happens, we note ([Fig. 14](#) ) that the horizontal q patterns are strongly asymmetric in the meridional direction, showing mushroomlike shapes with southern filaments longer and thinner than northern ones. These mushroom filaments are rather shallow features. This suggests an active horizontal advection, which is able to entrain and deform the scalar q field across the mean jet axis. Like at initial times, the vertical section shows that extremal q values are still concentrated in the northern region with a shallow pycnocline, while much weaker values predominate south of the main frontal axis.

The previous results show clearly that the mesoscale features, which are resulting from pure instability mechanisms, are meridionally asymmetric. In particular, the EPV distribution reveals that when an anticyclonic meander grows and deforms to the northwest, in general, a pinched-off anticyclonic eddy can be formed. In contrast, when a cyclonic meander deforms and moves to the southwest, it usually degenerates in thin filaments, which are dissipated before any coherent cyclonic eddy can be formed. This asymmetrical behavior can be explained through the following argument:

Consider a sketch of the density distribution across the jet ([Fig. 15](#) ) and consider the same cylindrical volume of fluid at two distinct positions between isopycnal surfaces ρ_1 and ρ_2 . In the absence of energy and momentum dissipation and forcing, the EPV is conserved between the two positions. It is readily seen that the first two terms on the rhs of [\(18\)](#) are much smaller than the last one (because $\text{Ri}^{-1} = (u_z^2 + v_z^2)/N^2 \ll 1$, with Ri the Richardson number) so that the EPV conservation equation becomes approximately

$$\frac{Dq}{Dt} \approx \frac{D}{Dt} \left[\frac{f + \xi}{\rho} \frac{\partial \rho}{\partial z} \right] = 0. \quad (19)$$


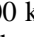
Applying [\(19\)](#) to a given cylindrical fluid volume of thickness h between two isopycnals ρ_1 and ρ_2 allows us to recover the familiar vorticity equation



$$\frac{D\xi}{Dt} = q_p \frac{Dh}{Dt} - \beta v, \quad (20)$$

where

Comparing the stretching and beta terms on the rhs of (20) it appears that the former dominates the evolution of relative vorticity. We may then write between the two positions of the fluid parcel that

$$\delta\xi \approx q_\rho \delta h. (22)$$

To zero order, the EPV of the basic state (Fig. 13 ) can be used in (22) to predict the vorticity changes. This state is strongly antisymmetric because both relative vorticity is low and thickness high on the southward flank of the jet, while the converse is true on the northern flank, leaving low (high) EPV to the south (north) of the jet. Consider now a particle moving northward while preserving its initial low q_ρ^S . It gains negative vorticity $\xi^- \equiv q_\rho^S \delta h$. Similarly, a particle moving southward will gain positive vorticity $\xi^+ \equiv q_\rho^N \delta h$. Now, the ratio of the gain in relative vorticity is in absolute values $\xi^-/\xi^+ = q^S/q^N$, a ratio smaller than unity from the basic-state distribution. Mass conservation further indicates that negative (positive) relative vorticity found north (south) of the jet is associated with large (small) areas. Henceforth, the basic EPV distribution favors a distribution of large-scale, relatively weak anticyclones north of the jet as compared to smaller scale and stronger cyclones south of the jet. What is observed is that as the instability evolves, the meanders grow and tend to wind around the upstream adjacent meander (with opposing vorticity). Through this, both anticyclonic and cyclonic filaments tend to form, with the difference that anticyclonic filaments are horizontally large and weak, while the cyclonic ones are horizontally thin and strong. Later on, an anticyclonic filament that has penetrated far northward is able to pinch off without losing its identity, while the thinner cyclonic ones are apparently more sensitive to mixing processes that are able to dissipate them before becoming coherent structures. Indeed, the numerical simulation reveals that anticyclones have typical diameters of 150 km, while typical cyclonic filaments have lengths of 150 km and widths of about 40 km. For a biharmonic subgrid dissipation scheme (with $K_H = 10^{10} \text{ m}^4 \text{ s}^{-1}$), we see that the corresponding dissipation timescales ($T_{\text{damp}} = L^4/(\pi^4 K_H)$) are of 16 years for anticyclones, but only around 30 days for the cyclonic filaments, a small value due to the extremely selective dissipation of the biharmonic. Thus, the arguments based on the initial EPV distributions along with dissipation suggest that anticyclones found north of the jet can survive until an interaction with an eastward propagating meander is produced, leading to a pinched-off eddy, while cyclonic filaments dissipate too quickly. It is also clear now that the oscillation pattern observed in the spectral amplitude of the \mathbf{u} field for wavelengths between 100 and 200 km (Fig. 6 ) corresponds to this degeneration process of cyclonic meanders into cyclonic filaments. The reason why the instability leads to asymmetric patterns is therefore entirely due to the initial EPV distribution of the basic state, caused by the shallowing of the pycnocline. Although such asymmetries are not new in PE modeling of jets (Wood and Ikeda 1994), its importance for the dynamics of the eddy-mean flow interaction merits emphasis. These findings allow us to explore the robustness of this ring/meander asymmetric distribution. In other words, enhanced production and survival rate of pinched-off anticyclones relatively to the almost nonexistent pinched-off cyclones as well as large anticyclonic meanders against thin cyclonic meanders must be stressed as going along with EPV asymmetry. With this in mind, several sensitivity tests have been performed to ascertain which factors can affect this meridional asymmetric ring production. Runs with and without the beta effect showed that β contributes to the jet coherency and stability and reduces the growth rate of the meanders. Although it has the right distribution to enhance the meridional asymmetry of the vorticity distribution, the effect is completely negligible compared to the meridional thickness distribution. Because of the strong effect of the biharmonic, several runs have also been carried out with Laplacian in place of biharmonic operators in both momentum and tracer equations. Although this has the effect of weakening the eddy field, the asymmetry distribution and production/survival rate between cyclones and anticyclones remains, and our previous arguments suggest that it is likely to persist at various spatial resolutions on the grounds of selective dissipation of the smaller-scale cyclones. The effect of vertical mixing is negligible at these eddy timescales and its absence did not change the results. The last parameter that was varied (see section 3) is the relaxation timescale toward the initial basic state. Although small relaxation reduces the mesoscale turbulence and the production of coherent structures by weakening the reservoir of available potential energy, it appears that the meridional asymmetry with dominance of the anticyclonic meanders is always present.

Since the asymmetry appears so obvious in the model simulations, it is worth looking back briefly at the observations. The Kielmann and Käse (1987) sketch of the southern temperature front, 18° to 16°C, from the NOAA-7 satellite infrared picture (their Fig. 1b ) shows that meridional asymmetry is present through a northwestward deformation of anticyclonic meanders. Furthermore, the observed horizontal meander scale (~220 km) agrees quite well with the scale of 240 km reached at finite amplitude in the channel model. Like the observed noncircular “warm” (anticyclonic) eddy of Kielmann and Käse (1987), the model similarly produced a noncircular anticyclonic feature, resulting from nonlinear interaction between an almost circular anticyclonic eddy and an anticyclonic meander (Figs. 7b and 7c ). The enhanced mesoscale activity north of the jet is also supported by Le Traon and De Mey's analysis (1994) using 2 years of Geosat altimetric data, and we suggest the instability of the Azores jet as the cause of this mesoscale activity (instead of their suggestion of wind-forced Rossby waves at the Gulf of Cadiz).

5. Energetics and dominant instability

A complementary understanding of the origin of mesoscale turbulence and of its interaction with mean flows can be achieved through an energy analysis. Because of the “atmospheric” periodic geometry of our channel, “zonal means” are suitable and will be denoted by an upper bar. Therefore, the description of the eddy–mean flow interaction requires the knowledge of conservation equations for the zonal-mean and eddy kinetic energies, as well as for the gravitational potential energy. These are discussed globally after spatially averaging over the entire volume of the fluid.

Writing

$$\langle \dots \rangle = \frac{1}{L_y H} \int_{-H}^0 \int_0^{L_y} \dots dy dz, \quad (23)$$

where L_y and H are, respectively, the meridional extent and depth of the model channel and making use of the periodicity condition allows is to write the conservation equation for total mean kinetic energy ($\overline{\text{KE}}$):

$$\begin{aligned} & \frac{d}{dt} \left\langle \frac{\rho_0}{2} (\overline{u^2} + \overline{v^2}) \right\rangle \\ &= -\rho_0 \left\langle \overline{u} \left(\frac{\partial}{\partial y} \overline{v'u'} + \frac{\partial}{\partial z} \overline{w'u'} \right) + \overline{v} \left(\frac{\partial}{\partial y} \overline{v'v'} + \frac{\partial}{\partial z} \overline{w'v'} \right) \right\rangle \\ & \quad - g \langle \overline{w\rho} \rangle + \rho_0 \left\langle k_H \left(\overline{u} \frac{\partial^4 \overline{u}}{\partial y^4} + \overline{v} \frac{\partial^4 \overline{v}}{\partial y^4} \right) + \frac{\partial k_v}{\partial z} \left(\overline{u} \frac{\partial \overline{u}}{\partial z} + \overline{v} \frac{\partial \overline{v}}{\partial z} \right) \right. \\ & \quad \left. + k_v \left(\overline{u} \frac{\partial^2 \overline{u}}{\partial z^2} + \overline{v} \frac{\partial^2 \overline{v}}{\partial z^2} \right) \right\rangle \\ & \quad + \frac{\rho_0}{T_d} \langle (\overline{u} \overline{u}_{\text{clm}} + \overline{v} \overline{v}_{\text{clm}}) - (\overline{u^2} + \overline{v^2}) \rangle. \end{aligned} \quad (24)$$

Also, the conservation equation for total eddy kinetic energy (KE') will read

$$\begin{aligned} & \frac{d}{dt} \left\langle \frac{\rho_0}{2} (\overline{u'^2} + \overline{v'^2}) \right\rangle \\ &= \rho_0 \left\langle \overline{u} \left(\frac{\partial}{\partial y} \overline{u'v'} + \frac{\partial}{\partial z} \overline{u'w'} \right) + \overline{v} \left(\frac{\partial}{\partial y} \overline{v'v'} + \frac{\partial}{\partial z} \overline{v'w'} \right) \right\rangle \\ & \quad - g \langle \overline{w'\rho'} \rangle \\ & \quad + \rho_0 \left\langle k_H (\overline{u' \nabla_H^4 u'} + \overline{v' \nabla_H^4 v'}) + k_v \left(\overline{u' \frac{\partial^2 u'}{\partial z^2}} + \overline{v' \frac{\partial^2 v'}{\partial z^2}} \right) \right. \\ & \quad \left. + \frac{\partial k_v}{\partial z} \left(\overline{u' \frac{\partial u'}{\partial z}} + \overline{v' \frac{\partial v'}{\partial z}} \right) \right\rangle - \frac{\rho_0}{T_d} \langle (\overline{u'^2} + \overline{v'^2}) \rangle, \end{aligned} \quad (25)$$

while the conservation equation for total gravitational potential energy (PE) is

$$\begin{aligned} \frac{d}{dt}\langle \rho g z \rangle &= g\langle \bar{\rho} \bar{w} \rangle + g\langle \bar{\rho}' w' \rangle \\ &- g\left\langle \bar{\rho} \frac{\partial k_v^p}{\partial z} + 2k_v^p \frac{\partial \bar{\rho}}{\partial z} - \frac{\partial}{\partial z} \left(k_v^p \frac{\partial}{\partial z} (\bar{\rho} z) \right) \right\rangle \\ &- \frac{g}{T_d} \langle z(\bar{\rho} - \rho_{\text{clm}}) \rangle. \end{aligned} \quad (26)$$

Equations (24)–(26) may be rewritten, symbolically, according to the physical meaning of its interaction terms. Each term on the rhs represents energy transfers between different energy forms. Following the order in the previous equations, this is

$$\begin{aligned} \frac{d}{dt}(\overline{\text{KE}}) &= -(\overline{\text{KE}} \rightarrow \text{KE}') - (\overline{\text{KE}} \rightarrow \text{PE}) \\ &+ (\text{EU} \rightarrow \overline{\text{KE}}) + (\overline{\text{KE}} \rightarrow \text{clm}) \end{aligned} \quad (27)$$

$$\begin{aligned} \frac{d}{dt}(\text{KE}') &= (\overline{\text{KE}} \rightarrow \text{KE}') - (\text{KE}' \rightarrow \text{PE}) \\ &+ (\text{EU} \rightarrow \text{KE}') - (\text{KE}' \rightarrow \text{clm}) \end{aligned} \quad (28)$$

$$\begin{aligned} \frac{d}{dt}(\text{PE}) &= (\overline{\text{KE}} \rightarrow \text{PE}) + (\text{KE}' \rightarrow \text{PE}) \\ &- (\text{EU}^p \rightarrow \text{PE}) - (\text{PE} \rightarrow \text{PE}_{\text{clm}}), \end{aligned} \quad (29)$$


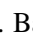
where $(P_1 \rightarrow P_2)$ means conversion of P_1 energy type into energy P_2 . With this rule, $(\overline{\text{KE}} \rightarrow \text{KE}')$ is transfer of kinetic energy from the mean to the eddy field via Reynolds stress, $(\text{PE} \rightarrow \overline{\text{KE}})$ and $(\text{PE} \rightarrow \text{KE}')$ represents the gain of mean and eddy kinetic energy through gravitational potential energy conversion. Since $(\text{EU} \rightarrow \overline{\text{KE}})$ and $(\text{EU} \rightarrow \text{KE}')$ are negative, they represent the gain of internal energy through viscous dissipation of mean and eddy kinetic energy that, in the absence of wind or other surface stress forcing, acts always as a sink term, while $-(\text{EU}^p \rightarrow \text{PE})$ is the gain of potential energy through subgrid vertical eddy diffusion (always in this positive sense for a stable stratified fluid and so acts like a source term). $(\text{clm} \rightarrow \overline{\text{KE}})$ and $(\text{clm} \rightarrow \text{KE}')$ are the gain of mean and eddy kinetic energy through the climatological forcing and $(\text{PE} \rightarrow \text{PE}_{\text{clm}})$ the conversion between gravitational potential energy of actual and climatological fields. Since the basic-state field is always kept constant, the associated $\overline{\text{KE}}_{\text{clm}}$, KE'_{clm} , and PE_{clm} values also remain constant, in particular for the total domain volume V , $\overline{\text{KE}}_{\text{clm}} = \rho_0 V(u_{\text{clm}}^2 + v_{\text{clm}}^2)/2$, $\text{KE}'_{\text{clm}} = 0$, and $\text{PE}_{\text{clm}} = Vgz\rho_{\text{clm}}$. This means that the terms of (27) to (29) containing clm are not pure transfers but are source or sink terms. Since we always have $(\text{KE}' \rightarrow \text{clm}) > 0$, then the restoring forcing to climatology acts like an eddy kinetic energy sink that will reduce instabilities. The remaining terms $(\overline{\text{KE}} \rightarrow \text{clm})$ and $(\text{PE} \rightarrow \text{PE}_{\text{clm}})$ may, on the other hand, have either sign.

b. Time evolution energetics

In order to characterize the different phases of the simulations, an intensive analysis of the model run energetics has been performed. Figure 16 represents the evolution of mean and eddy kinetic energies, $\overline{\text{KE}}$ and KE' , and available potential energy APE, (which is defined as the difference between the total potential energy at a given time, PE, and the constant total potential energy of the climatological state, PE_{clm}). During the first month or so, there is little energy exchange but as soon as instability is triggered, around day 50, an important decrease of APE happens along with an increase of KE' , until around day 130. Two peaks of KE' are visible around days 125 and 175, which coincides with the pinch-off of the two anticyclones. After day 175, APE starts to increase again, while KE' is decreasing, indicating that the first instability cycle is attaining a minimum and that a statistical equilibrium between the turbulence production and the return to climatology is

trying to be established. At this stage, climatology starts to win competition with mesoscale turbulence, the APE reservoir starts to refill, and a new maximum of APE, happening around day 300, tends to coincide with a KE' minimum. At this secondary APE maximum, a new instability cycle starts and around day 350 the instability that feeds on APE is at its maximum (KE' maximum) so that a vacillation cycle of about 200 days (between APE maximums or KE' minimums) appears. The mean \overline{KE} always starts to increase after a KE' maximum and attains its relative maximum point half way of the APE recovering period. For a longer integration period (up to day 1200) the described pattern will repeat itself and the 200-days cycle is the only notable feature. The initial APE level will not be recovered again, it will be eroded by instabilities prior to attain the departure level. This is the reason why we concentrate all our analysis effort in the first cycle when the APE levels start at the observed AzC levels. Without a background restoring climatology, only the first cycle will take place and instabilities will almost completely die out after about day 300. A detailed analysis of the conversion terms of [Eqs. \(27\)–\(29\)](#) shows immediately the operative physical mechanisms along the time evolution. Looking first at the eddy kinetic energy transfer, we observe successively (Fig. 17).

1) The instability growth phase for the first 100 days is dominated by a direct conversion of PE into KE', indicating clearly that baroclinic instability governs the evolution. The return to climatology acts as an efficient sink of KE', limiting the maximum growth of perturbations.

2) At later times (after 100 days), the mean kinetic energy \overline{KE} is fed periodically by eddy kinetic energy through Reynolds stress convergence. This interaction has a period of around 40–50 days. Note that the maximum peaks of this transfer occurs at the end of an intense (PE \rightarrow KE') decrease, which means that potential energy conversion declines when the eddy kinetic energy feeds the mean energy. The two relative minima of $(\overline{KE} \rightarrow KE') < 0$ ([Fig. 17](#) ) , which take place around days 125 and 175, occur when anticyclonic eddies are produced. The periodic behavior of these transfer terms shows that PE is feeding \overline{KE} via the indirect route of the Reynolds stresses, a result that agrees with those of [Ikeda \(1981\)](#), [Simmons and Hoskins \(1980\)](#), and [Wood \(1988\)](#). We may then quantify the energy sources for the eddies. Their growth depends on the two energy conversion mechanisms from mean kinetic and/or mean potential to eddy kinetic energy: $(\overline{KE} \rightarrow KE') > 0$ and $(PE \rightarrow KE') > 0$, that is, respectively, barotropic and baroclinic instability, present in the conservation [equation \(28\)](#). The other terms, climatological forcing and dissipation, are sinks of eddy kinetic energy. It has been observed that $(PE \rightarrow KE')$ is always positive, while $(\overline{KE} \rightarrow KE')$ is slightly positive only for a few very short periods of time. We then conclude that the instability is strongly dominated by the baroclinic instability. The relative weight of the two instability mechanisms as a percentage contribution for the total variability in $d(KE')/dt$ is shown in [Fig. 18](#) . Baroclinic and barotropic instability percentage, respectively %IBC and %IBT, are calculated as


$$\%IBC = \frac{(PE \rightarrow KE')}{SKE'}, \quad (30)$$

and

$$\%IBT = \frac{(\overline{KE} \rightarrow KE')}{SKE'}, \quad (31)$$

where

$$SKE' = |(\overline{KE} \rightarrow KE')| + |(PE \rightarrow KE')| + |(EU \rightarrow KE')| + |(KE' \rightarrow \text{clm})|. \quad (32)$$

Note that baroclinic instability contributes at all times to produce eddy kinetic energy and is very important initially (80%), while barotropic instability appears possible only for brief periods (days 150 to 160, 190 to 220, and 265 to 280). This is to say that, most of the time, barotropic instability is absent and that, on the contrary, the eddies transfer kinetic energy to the mean flow through the Reynolds stresses. For the time period of one year (40–400 days), excluding the initial phase of spinup (0–40 days), a block energy diagram for the energy transfer summarizes the situation ([Fig. 19](#) ). This block energy diagram indicates the following balances:

$$\frac{d}{dt}(\overline{KE} + KE' + PE) = \text{forcing} + \text{dissipation}, \quad (33)$$


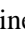
where

$$- (\text{PE} \rightarrow \text{PE}_{\text{clm}}), \quad (34)$$

and

$$\begin{aligned} \text{dissipation} = & (\text{EU} \rightarrow \overline{\text{KE}}) + (\text{EU} \rightarrow \text{KE}') \\ & - (\text{EU}^p \rightarrow \text{PE}). \end{aligned} \quad (35)$$

The boxes are energy reservoirs for the total domain, the arrows between them are energy fluxes, while the external arrows represent forcing and dissipation. Clearly, baroclinic instability feeds KE' reducing $\overline{\text{KE}}$, while KE' is feeding $\overline{\text{KE}}$. In other words, eddy rectification occurs to generate mean flows, while climatological forcing is the most important eddy kinetic energy sink.

[Rhines \(1979\)](#) has shown that an unstable baroclinic situation evolves in the long term toward a more barotropic state where perturbations get in phase in the vertical. To compare with his free decay experiments, an index of barotropy has been computed as the ratio of barotropic kinetic energy to total kinetic energy ([Fig. 20](#) ). As soon as the instability is initiated, the index increases in agreement with Rhines results, but here an equilibrium value of roughly 60% is obtained, caused by the competition between baroclinic instability and the climatological forcing that enables the jet to survive in time. When climatology is removed, return to barotropy due to baroclinic instability becomes larger than 90% after 250 days. So conversion from a baroclinic to barotropic mode is still taking place when the restoring to a mean climatology is present. However, the barotropization process is often interrupted and may even reverse at times (e.g., period 200–300 days in [Fig. 20](#) ). This kind of partition between the energy of barotropic and baroclinic modes is often observed in the midlatitudes of the ocean interior ([Wunsch 1997](#)). Surface wind forcing is hard put to explain this signature because it generates mostly a barotropic response, unless small structure in the wind field or in the bottom floor is invoked ([Tréguier and Hua 1988](#)). The present results may well provide a reasonable alternative based on the local baroclinic instability that develops intermittently along oceanic jets. Of course, these jets are part of the general circulation and the important question arises as to the role of these eddies in the maintenance of the structure of the jets themselves, a point that is the subject of the next section.


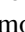

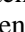
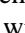
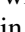
6. Zonal mean flow dynamics



A zonal mean flow analysis has been performed in order to evaluate whether or not the geostrophic turbulence is able to drive persistent mean flow patterns, which in turn are able to modify significantly the initial basic state. To separate the geostrophic contribution in the velocity field, we have defined geostrophic velocities \mathbf{v}_g as the velocities whose Coriolis accelerations balance the pressure gradient terms. With this definition, the zonal means become


$$\overline{u}(y, z, t) = \overline{u}_g(y, z, t) + \overline{u}_{\text{ag}}(y, z, t) \quad (36a)$$

$$\overline{v}(y, z, t) = \overline{v}_{\text{ag}}(y, z, t) \quad (36b)$$

$$\overline{w}(y, z, t) = \overline{w}(y, z, t). \quad (36c)$$

Carrying out this zonal averaging, an eastward current transporting between 10.7 and 14.5 Sv appears, while northward of the main jet a westward persistent countercurrent appears with a transport ranging from 2.2 to 6 Sv, thus preserving the total channel transport of 8.5 Sv. This is in agreement with the climatological results previously presented in [section 2](#). While this is hardly surprising for the main eastward jet that is explicitly forced by our model, the novel result is that the instability dynamics of the model reproduces the westward current that was intentionally absent in our initialization. The countercurrent starts around day 75, is a permanent feature during all the mesoscale instability period, and its subsurface structure is the result of a well-developed zonal westward flow. The eastward main jet, which starts at the channel central latitude broadens somewhat and migrates toward the south some 30 km during the mesoscale instability period ([Fig. 21](#) ). The time and zonally averaged jets ([Fig. 22](#) ) show transports of, respectively, 13 Sv to the east and 4.5 Sv to the west, in good agreement with the annual figures of [Table 1](#) . Note that the baroclinic structure of the main jet has weakened, when compared with the initial state ([Fig. 4](#) ) and that, simultaneously, the countercurrent has appeared with a subsurface maximum around 600 m. Comparing model-generated zonal mean structures ([Fig. 22](#) ) with the equivalent climatological results ([Fig. 2](#)  in summertime), we note a surprising similarity not only for AzC and AzCC signals but also for E1 and E2 structures.

Turning to the circulation that occurs in the meridional plane, consider first the vertical velocity at the depth of its maximum (370 m). A mean upwelling dominates at the jet axis ([Fig. 23](#) ), while downwelling dominates at both south and north AzC flanks. Note that between days 100 and 130 the upwelling is split in two bands. Fifty-day time means (between days 100 and 150 and days 150 and 200) of the meridional ageostrophic circulation vector are shown in [Fig. 24](#) ,

exhibiting a clear dipolar structure. Maximum vertical and horizontal mean speeds are about 0.5 and 90 m/day, respectively. When a longer integration is considered, we note that this dipole with upwelling in the center and downwelling at the sides is vacillating between two states, with either one central upwelling band (e.g., [Fig. 24](#)  between days 150 and 200) or two well-separated cells (e.g., between days 100 and 150), although after day 200 dipole intensities decrease relatively to the first instability cycle. This is consistent with the vertical distribution shown previously. The vacillation between these two meridional dipole states is roughly about 50 days. However, it is important to mention that this dipolar structure is a persistent feature in time, existing for the zonal mean at any time during the instability cycle. So the numerical simulation provides us with two novel mean structures, a westward countercurrent north of the jet and a dipolar ageostrophic circulation with central upwelling. Of course and consistent with energetics, the eddies are expected to play a major role in the generation of these structures. Because of the essentially “atmospheric” geometry of our simulations, we study the eddy–mean flow interaction from the point of view of the Eliassen–Palm fluxes using the transformed Eulerian mean equation (TEM) first used by [Edmond et al. \(1980\)](#) to understand the relation between eddy activity and changes in the tropospheric mean jets [see also [Andrews et al. \(1987\)](#)]. For the present flat-bottom simulation without direct atmospheric forcing, geostrophic turbulence appears as the end product of baroclinically unstable waves, as was shown in [section 5](#). Now, in order to be able to identify the mechanisms that are generating permanent mean features like the countercurrent, the TEM proved valuable. Casting them in our primitive equations formalism, we found that, to a very good approximation, the dominant terms reduced to

$$\frac{\partial \bar{u}}{\partial t} \cong f \bar{v}_{\text{ag}}^* + \frac{1}{\rho_0} \nabla \cdot \mathbf{F} - \frac{1}{T_d} (\bar{u} - u_{\text{clm}}) \quad (37)$$

$$f \bar{u} \cong -\frac{\partial \bar{\phi}}{\partial y} \quad (38)$$

$$\frac{\partial \bar{\rho}}{\partial t} \cong -\bar{w}^* \frac{\partial \bar{\rho}}{\partial z} - \frac{1}{T_d} (\bar{\rho} - \rho_{\text{clm}}), \quad (39)$$


where \mathbf{F} , the Eliassen–Palm flux, is


$$\mathbf{F} = \left[0, \left(\rho_0 \frac{\bar{u}_z}{\bar{\rho}_z} \overline{v' \rho'} - \rho_0 \overline{v' u'} \right), \left(\rho_0 \frac{f + \bar{\xi}}{\bar{\rho}_z} \overline{v' \rho'} - \rho_0 \overline{w' u'} \right) \right] \quad (40)$$

in which $\bar{\xi} = -\partial \bar{u} / \partial y$ and $(\bar{v}_{\text{ag}}^*, \bar{w}^*)$ is the residual meridional circulation defined as

$$\bar{v}_{\text{ag}}^* = \bar{v}_{\text{ag}} - \frac{\partial}{\partial z} \left(\frac{\overline{v' \rho'}}{\bar{\rho}_z} \right) \quad (41)$$



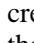

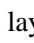
$$\bar{w}^* = \bar{w} + \frac{\partial}{\partial y} \left(\frac{\overline{v' \rho'}}{\bar{\rho}_z} \right). \quad (42)$$

For the TEM set [\(37\)–\(39\)](#), all the unstable wave or eddy effects are represented, exclusively, through the Eliassen–Palm (EP) flux vector divergence, which is a zonal force per unit mass exerted by the unstable waves or eddies on the mean flow. If the disturbances are steady and linear within a conservative flow, then the divergence of this EP flux (which is also the meridional potential vorticity flux) and the residual circulation will both vanish, leading to the Charney–Drazin’s nonacceleration theorem. When negative (positive) the divergence of the EP flux in the meridional plane will decelerate (accelerate) the eastward flow. It is also interesting to note that in the TEM system [\(37\)](#) and [\(39\)](#) the \bar{u} and $\bar{\rho}$ fields would change, independently, through the sole actions of the EP flux vector divergence and forcings, thus destroying a priori the zonal-mean geostrophic balance. Then the mean residual circulation can be seen as necessary to maintain the zonal-mean thermal wind relation. We can now apply [\(37\)](#) to our zonal jet. At a given time, we find that the Coriolis and the EP flux divergence forces dominate the \bar{u} time rate of change. In fact, adding them together results in good comparisons with direct calculations of $\partial \bar{u} / \partial t$. [Figure 25](#)  shows such a result at day 110. We see that the Coriolis force acting over the residual circulation contributes in a major way to the deeper signature of the westward countercurrent, because the sum of the two

dominant terms has the same structure as the Coriolis force, $f\mathbf{v}_{ag}^*$. The surface signal, however, is dominated by the EP flux vector divergence. Looking now at the main eastward jet, it appears that its migration to the south is caused by the divergence of the EP flux. Note how the divergence of the EP flux over the main part of the zonal mean jet tends to increase barotropy, while the Coriolis force does the opposite. These same results are valid during the whole instability cycle, although with changing intensity. This can be illustrated by the time evolution of the EP flux at a given level ($z = 114$ m in [Fig. 26](#) ) , where the presence of a persistent deceleration zone biased toward the northern flank of AzC, created by the eddy activity concentration, is able to reverse the general eastward flow and create the upper (above 250 m) westward signature of AzCC. Similarly, the midwater depth maximum and the deep signature of this westward flow are persistently built in time by the Coriolis force acting on the meridional residual circulation. The eddy mechanism that we propose for the maintenance of the AzCC must be contrasted with [Onken's \(1993\)](#) proposal to resolve this issue with wind forcing.

In order to understand how the momentum and eddy buoyancy fluxes combine and cause these acceleration/deceleration patterns, the dominant terms of the EP vector divergence are developed as

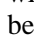
$$\frac{1}{\rho_0} \nabla \cdot \mathbf{F} \approx -\frac{\partial}{\partial y} \overline{v'u'} + \frac{f + \bar{\xi}}{\bar{\rho}_z} \frac{\partial}{\partial z} \overline{v'\rho'}. \quad (43)$$

Since the spatial distribution of the dominant terms in [\(37\)](#) does not evolve in time (e.g., [Fig. 26](#) ) , we consider, for example, the 50-day time mean between day 100 and 150. The distribution of terms on the right-hand side of [\(43\)](#) ([Fig. 27](#) ) shows that the Reynolds stress divergence is associated with the northern eddy activity propagation through the creation of a mean convergence zone for \mathbf{F} at the surface. The $\overline{u'v'}$ correlation ([Fig. 28](#) ) is negative over the main part of the jet so that the upper northern (southern) flank is a region of divergence (convergence) of the Reynolds stresses $\overline{u'v'}$ ([Fig. 27](#) ) . The eddies sharpen the mean horizontal shear in the sense of negative viscosities. Indeed, north (south) of the jet, there is an upgradient (downgradient) transport of zonal momentum. This is associated through [\(24\)–\(25\)](#) with kinetic energy transfers from the eddy to the mean, north of the jet axis, the opposite being true south of the jet axis (note how different this is from a barotropic instability mechanism that would rely on mean kinetic energy as a primary energy source, in which case $\overline{u'v'}$ would develop positive and negative values, respectively, north and south of the jet). It appears, therefore, that this pervasive distribution of negative $\overline{u'v'}$ correlation is of crucial importance for the rectification in the upper layers. This distribution agrees fully with the southeast–northwest meander deformation observed in [Fig. 7](#) ) and is the statistical result of the already described meridional asymmetry. To stress the connection, remember that meridional asymmetry is the result of a northern dominance of negative vorticity anomalies. Such vorticities have been acquired by northward moving parcels while conserving their potential vorticity, so it is plausible that $\mathbf{v}'\xi'$ is negative in that region. But, since

$$\overline{v'\xi'} = -\frac{\partial}{\partial y} \overline{v'u'}, \quad (44)$$

then we have

$$\overline{v'u'}(y, z) = \int_y^{y_{\text{north}}} \overline{v'\xi'} dy, \quad y < y_{\text{north}}. \quad (45)$$

Thus, if $\mathbf{v}'\xi' < 0$ is expected on the northern side, integration from the north away from the eddy activity shows that $\overline{u'v'}$ will be predominantly negative everywhere. Because $\overline{u'v'}$ must also go to zero away to the south, $\mathbf{v}'\xi'$ must change sign and become positive south of the jet ([Fig. 28](#) ) . The characteristic $\overline{u'v'}$ pattern, itself a consequence of meridional asymmetry of the jet, is then associated with the countercurrent generation driven by the eddy transport of westward momentum. As stressed by [Edmond et al. \(1980\)](#), when only the dominant terms in the EP divergence [\(43\)](#) are kept, one may show that it becomes identical with the meridional flux of eddy potential vorticity. It is readily seen that this potential vorticity flux is directed down the mean PV gradient, providing the main source of eddy potential enstrophy against dissipation, as suggested in other context by [Rhines and Holland \(1979\)](#).

To understand how the eddies drive the dipolar ageostrophic circulation, we now calculate both the passive and the residual circulation. The residual circulation is that part of the total meridional ageostrophic circulation that is able to change the mean flow, even in the absence of any eddy flux [if $\nabla \cdot \mathbf{F} = 0$ in [\(37\)](#), the mean flow is still able to change, but only due to the residual circulation or any nonturbulent forcing]. The passive circulation is that part of the total meridional ageostrophic circulation that is able to exactly cancel out the effect of the eddy fluxes into the mean flow, when $\nabla \cdot \mathbf{F} = 0$. After [\(41\)](#) and [\(42\)](#), the passive circulation is simply

$$\bar{v}_{\text{ag}}^0 = \frac{\partial}{\partial z} \left(\frac{\overline{v' \rho'}}{\bar{\rho}_z} \right) \quad (46)$$

$$\bar{w}^0 = -\frac{\partial}{\partial y} \left(\frac{\overline{v' \rho'}}{\bar{\rho}_z} \right). \quad (47)$$



Defining a residual streamfunction Ψ^* for the residual circulation as

$$\bar{v}_{\text{ag}}^* = -\bar{\Psi}_z^* \quad (48)$$



$$\bar{w}^* = \bar{\Psi}_y^*, \quad (49)$$

we combine (37) and (39) in a way to preserve geostrophic balance of the mean jet to obtain an Eliassen-type equation for Ψ^* . The meridional residual streamfunction obeys the following elliptic equation:

$$\begin{aligned} N^2 \bar{\Psi}_{yy}^* + f^2 \bar{\Psi}_{zz}^* + N_y^2 \bar{\Psi}_y^* \\ = \frac{f}{\rho_0} \frac{\partial}{\partial z} \nabla \cdot \mathbf{F} - f \frac{\partial}{\partial z} \frac{(\bar{u} - u_{\text{clm}})}{T_d} + \frac{g}{\rho_0} \frac{\partial}{\partial y} \frac{(\bar{\rho} - \rho_{\text{clm}})}{T_d}. \end{aligned} \quad (50)$$

This equation remains elliptical whenever gravitational stability conditions are maintained ($N^2 > 0$). Using the boundary conditions of zero normal velocity and [Adams \(1991\)](#) elliptical solver, the residual circulation may be readily calculated. Proceeding with the time average between day 100 and 150 for both the passive and residual circulation ([Fig. 29](#) ) , we can compute the parts that compose the ageostrophic meridional dipole [adding them together, a picture similar to [Fig. 24](#)  (days 100 to 150) will result, a useful way to check the decomposition]. Clearly, the northern downwelling branch of the ageostrophic meridional dipole is caused by the residual circulation, while the southern one is the result of passive circulation. The central upwelling band results from the sum of both upwelling branches of passive and residual circulation.

7. Conclusions

The Azores Current, a permanent shallow feature, flows eastward at 34°N. It represents a prototype for subtropical jets found on the poleward boundary of subtropical gyres. Associated with this jet and north of it, a westward countercurrent is found that transports about 2 Sv as compared with 13 Sv for the main eastward jet. Both flows reach their maximum in spring. The present study has examined the properties of the mesoscale turbulence generated by the instability processes of the jet and the manner in which the eddies feed back on the mean jet dynamics. To allow the development of realistic instabilities we have used a primitive equation model initialized with a jet structure reconstructed from a summer synoptic survey of the area. Because the main pycnocline shoals in a very short distance, potential vorticity shows near-surface extrema conducive to the instabilities and gives the flow its peculiar meridionally asymmetric character markedly different from QG calculations. The most unstable wavelength appears initially around 160 km, increasing to 240 km after the buildup of the eddy kinetic energy has occurred. The energetics have shown that the major instability has a baroclinic origin with mean potential energy feeding the eddies. These are able, in turn, to modify the mean flow and generate the westward countercurrent that was deliberately omitted from the initial state. The transport of the model countercurrent compares well with observations, and we therefore suggest that it is eddy driven. To support this conjecture, Eliassen–Palm flux decompositions are constructed. The EP flux vector is found to be much influenced by a pervasive $\overline{v'u}$ negative correlation that appears in an important part of the domain and is symptomatic of the meridional asymmetry of the turbulent field. This correlation is the statistical signature of a meridional asymmetry caused by the northwestward (southwestward) anticyclonic (cyclonic) meander deformation. The anticyclones are able to form coherent structures north of the jet axis, while cyclones found south of the jet axis cascade to smaller scales where they are dissipated. The dominance of anticyclones in these instability calculations provides another argument to explain their dominance in the real ocean. Similarity between our zonal mean model results ([Fig. 22](#) ) and the zonal mean climatological data results ([Fig. 2](#) ) , particularly in summer) strongly suggest that the observed countercurrent north of the Azores main jet, as well as the mean structures E1 and E2, are eddy driven. Since near the northern flank of the AzC the divergence of the EP flux is negative above 250 m, deceleration of the forced eastward jet occurs and the associated meridional density gradient reverses as soon as the countercurrent appears, forming thus the shallow signature of AzCC. Along with these upper-layer zonal mean modifications, a residual ageostrophic

circulation is forced by the vertical gradient of the EP flux vector divergence (50), forms in the meridional plane in order to maintain the thermal wind balance in the zonal direction. The Coriolis acceleration acting over this residual TEM meridional velocity drives the deeper signature of AzCC. We note that the vertical gradient of the EP flux vector divergence in the northern flank of AzC is, in turn, the result of a vertically changing form of AzC meanders, which have a smoother amplitude in depth (see Figs. 8a–c at 1050 m), producing a zonally coherent AzCC coincident with the westward circulation side of the cyclonic meanders. It is clear now that the northern circulation side of near-surface pinched-off anticyclones are producing the mean feature E1 (Figs. 2 and 22), while the westward circulation side of AzC anticyclonic meanders are producing the E2 feature. The northern flank of the jet warms at depth in a way similar to what is produced at the time of sudden stratospheric warming events described by Andrews et al. (1987). We also show that, in this instance, the meridional eddy potential vorticity flux is downgradient, maintaining eddy potential enstrophy against dissipation.

The total ageostrophic circulation (in the meridional depth plane) has a dipolar structure with mean upwelling reaching 0.5 m day⁻¹ and dominating near the jet axis with downwelling on either side. This dipole is the added result of the meridional residual circulation with the passive one and also bears its existence to the particular form of the $\mathbf{v}'u'$. It is not the result of climatological forcing terms, as it appears in free decay experiments as well (Alves 1996). In fact, all the described mean balances are obtained in the absence of nudged climatology either for the β - or f -plane cases (the dipole is even more intense but loses coherency as soon as the AzC jet loses its own, something that in our β -plane case happens around day 190 and for the f -plane around day 140). The meridional ageostrophic dipole and the AzCC are thus completely driven by mesoscale turbulence. We suggest that other midlatitude subtropical jets at the poleward boundary of subtropical gyres might well show similar eddy-driven countercurrent and secondary dipolar circulations in the meridional depth plane, two features intrinsically linked with the potential vorticity distribution of the basic state.

The results presented may have important consequences over future climatological sampling strategies since, according to them, mesoscale features must be resolved.

Acknowledgments

The authors gratefully acknowledge the helpful comments of Dr. M. Spall and an anonymous reviewer that contributed to the improvement of this final version. The first author gratefully acknowledges the support of the Junta Nacional de Investigação Científica e Tecnológica under Grant PRAXIS XXI/BD/3800/94. He also acknowledges all the support and encouragement he received during his stay at the Laboratoire de Physique des Océans, Université de Bretagne Occidentale, in Brest, France. This is a contribution of Azores University, Department of Oceanography and Fisheries and of the UMR 6523, partnership between CNRS, IFREMER and Université de Bretagne Occidentale, Brest, France.

REFERENCES

- Adams, J., 1991: MUDPACK: Multigrid software for linear elliptic partial differential equations. Version 3.0. National Center for Atmospheric Research, Boulder, Colorado, Scientific Computing Division User Document. [Available from NCAR, P.O. Box 3000, Boulder, CO 80307].
- Alves, M., 1996: Instability dynamics of a subtropical jet: The Azores Front–Current System case (FCA). Ph.D. thesis, Université de Bretagne Occidentale, Brest, France, 229 pp..
- , and A. Colin de Verdière, 1996: Instability of a subtropical jet—Application to the Azores Front–Current System. *Ann. Geophys.*, **14**, 386..
- , M. Juliano, J. Vitorino, J. Gonçalves, E. Isidro, and M. Encarnacion, 1993: Synoptic summer survey of azores front/current system, FCA, across and over Mid-Atlantic Ridge. *Proc. Conf. Int. on Thirteen Fisheries Week of Açores*, Horta, Azores, Azores Autonomous Government, 7pp..
- , A. Simões, A. C. de Verdière, and M. Juliano, 1994: *Atlas Hydrologique Optimale pour l'Atlantique Nord-Est et Centrale Nord (0°–50°W, 20°–50°N)*. Université des Açores, 76 pp..
- Andrews, D. G., J. R. Holton, and C. B. Leovy, 1987: *Middle Atmosphere Dynamics*. Int. Geophys. Ser., Vol. 40, Academic Press, 489 pp..
- Beckmann, A., 1988: Vertical structure of midlatitude mesoscale instabilities. *J. Phys. Oceanogr.*, **18**, 1354–1371.. [Find this article online](#)
- Bigg, G. R., 1990: Inversions of observations near the Azores front. *J. Mar. Res.*, **48**, 661–675..

Cromwell, D., P. G. Challenor, A. L. New, and R. D. Pingree, 1996: Persistent westward flow in the Azores Current as seen from altimetry and hydrography. *J. Geophys. Res.*, **101** (C5), 11 923–11 933..

De Mey, P., 1994: Optimal interpolation in a model of the Azores Current in 1986–1988. *Global Environmental Change*, NATO ASI Series, Series I, Springer-Verlag, 85–106..

Edmond, H. J., B. J. Hoskins, and M. E. McIntyre, 1980: Eliassen–Palm cross-sections for the troposphere. *J. Atmos. Sci.*, **37**, 2600–2616; 1981: Corrigendum, **38**, 1115.. [Find this article online](#)

Feliks, Y., and M. Ghil, 1996: Mixed barotropic-baroclinic eddies growing on an eastward midlatitude jet. *Geophys. Atmos. Fluid Dyn.*, **82**, 137–171..

Gill, A., E. J. S. A. Green, and A. J. Simmons, 1974: Energy partition in the large-scale ocean circulation and the production of mid-ocean eddies. *Deep-Sea Res.*, **21**, 499–528..

Haidvogel, D. B., and W. R. Holland, 1978: The stability of ocean currents in eddy resolving general circulation models. *J. Phys. Oceanogr.*, **8**, 393–413.. [Find this article online](#)

—, J. Wilkin, and R. Young, 1991: A semi-spectral primitive equation ocean circulation model using vertical sigma and orthogonal curvilinear horizontal coordinates. *J. Comput. Phys.*, **94**, 151–184..

Ikeda, M., 1981: Meanders and detached eddies of a strong eastward-flowing jet using a two-layer quasi-geostrophic model. *J. Phys. Oceanogr.*, **11**, 526–540.. [Find this article online](#)

Kielmann, J., and R. H. Käse, 1987: Numerical modeling of meander and eddy formation in the Azores Current frontal zone. *J. Phys. Oceanogr.*, **17**, 529–541.. [Find this article online](#)

Klein, B., and G. Siedler, 1989: On the origin of the Azores Current. *J. Geophys. Res.*, **94** (C5), 6159–6168..

Le Traon, P. Y., and P. De Mey, 1994: The eddy field associated with the Azores front east of the Mid-Atlantic Ridge as observed by the GEOSAT altimeter. *J. Geophys. Res.*, **99** (C5), 9907–9923..

Levitus, S., 1982: *Climatological Atlas of the World Ocean*. NOAA Prof. Pap. No. 13, 173 pp..

Maillard, C., and R. H. Käse, 1989: The near surface flow in the subtropical gyre south of the Azores. *J. Geophys. Res.*, **94**, 16 133–16 140..

Müller, T. J., and G. Siedler, 1992: Multi-year current time series in the eastern North Atlantic Ocean. *J. Mar. Res.*, **50** (1), 63–98..

Ollivault, M., 1995: La circulation générale de l'Atlantique Nord subtropical vers 700 m de profondeur, révélée par des flotteurs dérivants de subsurface. *C. R. Acad. Sci. Paris*, **321**, (Series II a), 153–160..

Onken, R., 1992: Mesoscale upwelling and density finestructure in the seasonal thermocline—A dynamical model. *J. Phys. Oceanogr.*, **22**, 1257–1273.. [Find this article online](#)

—, 1993: The Azores Countercurrent. *J. Phys. Oceanogr.*, **23**, 1638–1646.. [Find this article online](#)

Papoulis, A., 1965: *Probability, Random Variables, and Stochastic Processes*. McGraw-Hill, 583 pp..

Pedlosky, J., 1987: *Geophysical Fluid Dynamics*. 2d ed. Springer-Verlag, 710 pp..

Rhines, P. B., 1977: The dynamics of unsteady currents. *The Sea*. Vol. 6: *Marine Modelling*, E. D. Goldberg, I. N. McCave, Eds., Wiley Interscience, 189–318..

—, 1979: Geostrophic turbulence. *Annu. Rev. Fluid Mech.*, **11**, 401–441..

—, and W. R. Holland, 1979: A theoretical discussion of eddy driven mean flows. *Dyn. Atmos. Oceans*, **3**, 289–325..

Samelson, R. M., and D. C. Chapman, 1995: Evolution of a mixed layer front. *J. Geophys. Res.*, **100**, 6743–6759..

Schmitz, W. J., Jr., and M. S. McCartney, 1993: On the North Atlantic circulation, *Rev. Geophys.*, **31** (1), 29–49..

Simmons, A. J., and B. J. Hoskins, 1980: Barotropic influences on the growth and decay of nonlinear baroclinic waves. *J. Atmos. Sci.*, **37**, 1679–1684.. [Find this article online](#)

Spall, M., 1995: Frontogenesis, subduction, and cross frontal exchange at upper ocean fronts. *J. Geophys. Res.*, **100**, 2543–2557..

Stramma, L., and H. J. Isemer, 1988: Seasonal variability of meridional temperature fluxes in the eastern North Atlantic Ocean. *J. Mar. Res.*, **46**, 281–299..

—, and G. Siedler, 1988: Seasonal changes in the North Atlantic subtropical gyre. *J. Geophys. Res.*, **93** (C7), 8111–8118..

Treguier, A. M., and B. L. Hua, 1988: Influence of bottom topography on stratified quasi-geostrophic turbulence in the ocean. *Geophys. Astrophys. Fluid Dyn.*, **43**, 265–305..

Wang, D. P., 1993: Model of frontogenesis: Subduction and upwelling. *J. Mar. Res.*, **51**, 497–513..

Wood, R. A., 1988: Unstable waves on oceanic fronts: Large amplitude behavior and mean flow generation. *J. Phys. Oceanogr.*, **18**, 775–787.. [Find this article online](#)

—, and M. Ikeda, 1994: Comparison of mesoscale meanders and eddies simulated by quasi-geostrophic and primitive equation models: A case study. *J. Geophys. Res.*, **99** (C11), 22 645–22 663..

Wunsch, C., 1997: The vertical partition of oceanic horizontal kinetic energy. *J. Phys. Oceanogr.*, **27**, 1770–1794.. [Find this article online](#)

Tables

Table 1. AzC and AzCC associated zonal mean (25°–35°W) transports in Sv (1 Sv $\equiv 10^6 \text{ m}^3 \text{ s}^{-1}$) for each season and annual mean. The negative sign means flow toward the west. The maximum error is 1.0 Sv for AzC and 0.2 Sv for AzCC.

	Winter	Spring	Summer	Autumn	Annual
AzC	8.9	19.7	12.1	11.7	13.1
AzCC	-2.0	-3.0	-2.2	-0.8	-2.0

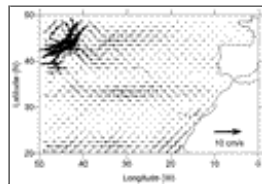
[Click on thumbnail for full-sized image.](#)

Table 2. Best-fit coefficients for (9) and (10).

Parameter	T	S
a_0	21.30175	2.13103
b_0	9.45×10^{-4}	2.105×10^{-3}
χ_0	0.00	35.0
d_0	3.85×10^{-2}	9.00×10^{-3}
g_0	-190.4762	-148.1482

[Click on thumbnail for full-sized image.](#)

Figures



[Click on thumbnail for full-sized image.](#)

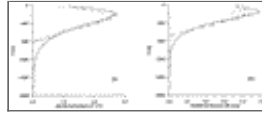
Fig. 1. Surface distribution of the annual mean thermal wind field referenced to 2000 dbar. To obtain the temperature (T) and salinity (S) fields, an optimal interpolation algorithm was used (Papoulis 1965), where the best field estimation, in a least square sense, is evaluated at a given grid point as a weighted sum of the surrounding data values. Assuming horizontal isotropy of the hydrological fields and choosing an integral correlation space scale of 600 km [twice the wavelength scale of observed mesoscale features and about half of that used by Levitus (1982)], the temperature and salinity optimal distributions, as well as their associated mean square errors, were then calculated (Alves et al. 1994). We may then calculate the surface distribution of the annual mean thermal wind field for the area referenced to 2000 m.





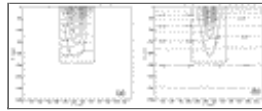
Click on thumbnail for full-sized image.

Fig. 2. Seasonal and annual zonal mean (between 25° and 35°W) is performed over the $u_g(x, y, z)$ thermal wind field. The resulting mean field for each season and annual mean is shown for the first 2000 m. Units are meters per second. Clearly there is an AzCC signal present through the four seasons. The E2 structure in summer may be seen as an Azores South Countercurrent. Solid (dashed) lines represent eastward (westward) flow.



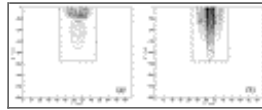
Click on thumbnail for full-sized image.

Fig. 3. $\Delta T(z)$ (a) and $\Delta S(z)$ (b) observed and its best fit for the north-south isobaric thermal and haline contrast. Dots represent original $\Delta T = T_{\text{south}} - T_{\text{north}}$ ($\Delta S = S_{\text{South}} - S_{\text{North}}$) and solid line is $\Delta T = a_0 z e^{b_0 z}$ ($\Delta S = c_0 z e^{d_0 z}$). The $a_0, b_0, c_0,$ and d_0 coefficient values may be seen in [Table 2](#).



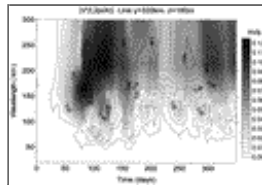
Click on thumbnail for full-sized image.

Fig. 4. Density field (dashed line) and thermal wind (solid) computed for the CODFRA/92 cruise (a) data and for the model basic state (b).



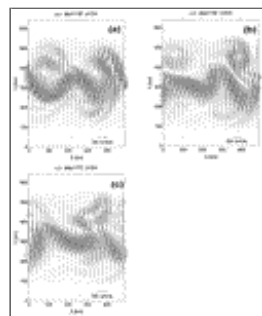
Click on thumbnail for full-sized image.

Fig. 5. The $\partial Q_B / \partial y$ interior for the Azores Current basic state in summer. Case (a) is for pure baroclinic instability [rhs of [Eq. \(15\)](#)] and case (b) is for pure barotropic instability [rhs of [Eq. \(16\)](#)]. Units are $\text{m}^{-1} \text{s}^{-1} \times 10^{12}$.



Click on thumbnail for full-sized image.

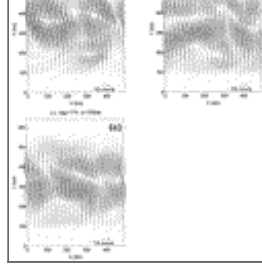
Fig. 6. Time evolution of zonal wavelength spectra for the demeaned and detrended \mathbf{U} field at the channel zonal axis line ($|V'(t, 2\pi/k_x)|$). Units are meters per second.



Click on thumbnail for full-sized image.

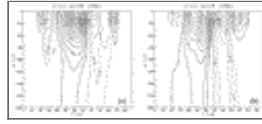
Fig. 7. Surface current patterns for the AzC model run. Case (a) is day 130, (b) day 150, and (c) day 170. The surface patterns are revealing a clearly enhanced anticyclonic production to the north of jet axis. To the south, only cyclonic filaments are visible.





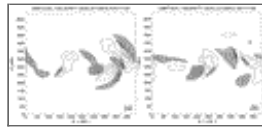
[Click on thumbnail for full-sized image.](#)

Fig. 8. Midwater depth (1050 m) current patterns for the AzC model run. Case (a) is day 130, (b) day 150, and (c) day 170. In depth we can see the formation of a coherent zonal countercurrent (AzCC) north of the AzC jet.



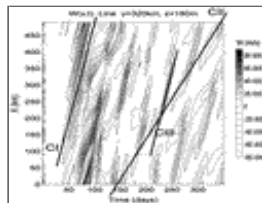
[Click on thumbnail for full-sized image.](#)

Fig. 9. Meridional cross sections of the zonal current component intensity, respectively, for day 150 (a) and day 170 (b) at a constant zonal position ($x = 350$ km) of the model run. Solid (dashed) lines represent the eastward (westward) flowing current.



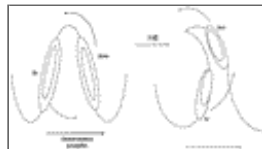
[Click on thumbnail for full-sized image.](#)

Fig. 10. Horizontal patterns of vertical velocity (in m s^{-1}) at level 180 m and for the day 130 (a) and 150 (b). Downwelling centers are shaded gray.



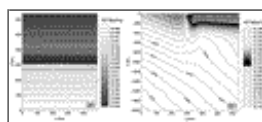
[Click on thumbnail for full-sized image.](#)

Fig. 11. Zonal phase propagation of mesoscale patterns along the jet axis line, revealed through the w field. Three classes of different phase propagation speeds are identified: $C_I \approx 5.3 \text{ km day}^{-1}$, $C_{II} \approx 2.4 \text{ km day}^{-1}$, and $C_{III} \approx 5.0 \text{ km day}^{-1}$. Upwelling is shaded gray.



[Click on thumbnail for full-sized image.](#)

Fig. 12. Cyclonically turning propagation of the up/downwelling centers in a deforming anticyclonic meander.



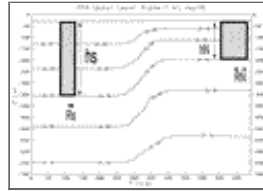
[Click on thumbnail for full-sized image.](#)

Fig. 13. Horizontal (a) ($z = 180$ m) and meridional (b) ($x = 350$ km) cuts of the basic state q field at day zero (EPV values shown must be multiplied by 10^{-9} to get $\text{m}^{-1} \text{ s}^{-1}$ SI units). White shade is for values smaller than -0.55 and greater than -0.45 .



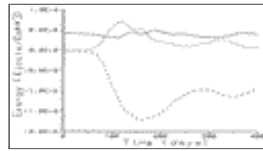
Click on thumbnail for full-sized image.

Fig. 14. Horizontal (a) ($z = 180$ m) and meridional (b) ($x = 350$ km) cuts of the q field at day 160. Gray shades and label codes as in Fig. 13.



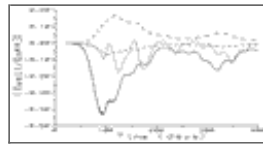
Click on thumbnail for full-sized image.

Fig. 15. Isopycnal cross-frontal distribution for AzC basic state. The isopycnal interval (26.10–26.70) has been chosen because it contains the main EPV signal. Note that the lightest density surfaces are almost flat planar according to observed and prototype summer AzC.



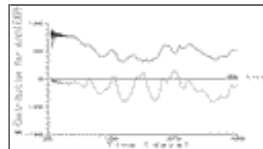
Click on thumbnail for full-sized image.

Fig. 16. Evolution of \overline{KE} (solid line), KE' (small dashed line), and APE (long dashed line) for the first 400 days of model run. Units are kJ km^{-3} . SI energy units are obtained multiplying actual values by 6.144×10^8 (the total volume of simulation domain).



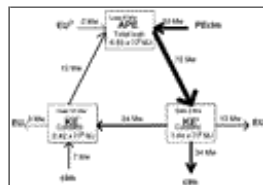
Click on thumbnail for full-sized image.

Fig. 17. Conversion terms of $d(KE')/dt$. Note that $(KE' \rightarrow PE) < 0$ (solid line), $(KE' \rightarrow \text{clm}) > 0$ (long dashed line), $(\overline{KE} \rightarrow KE')$ is mainly negative (small dashed line), while $(EU \rightarrow KE') < 0$ (medium dashed line). During the first 30 days, there is inertial/internal wave activity, which stops suddenly as soon as the explosive instability growing phase is triggered. This activity induces significant amplitude oscillation on $(KE' \rightarrow PE)$. Thus, the first 30 days have been removed in order to preserve curve clarity. SI power units are obtained multiplying actual values by 6.144×10^8 .



Click on thumbnail for full-sized image.

Fig. 18. Baroclinic instability dominates KE' generation in AzC system. Positive percentage means that contribution is for $d(KE')/dt > 0$, while negative percentage is for $d(KE')/dt < 0$. Solid (dashed) line is baroclinic (barotropic) instability.



Click on thumbnail for full-sized image.

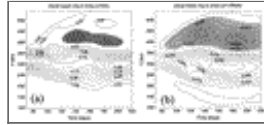
Fig. 19. Block energy diagram for 1-yr time mean period (days 40–400). We note that $\langle d(\overline{KE} + KE' + PE)/dt \rangle = 16 + 2 - 8 = 10$ Mw and $F + D = 7 - 34 + 50 - 3 - 12 + 2 = 10$ Mw. This sum is never zero because the system vacillates with about 200 days period due to a continuous competition between nudged forcing (F) and instability dissipation (D).





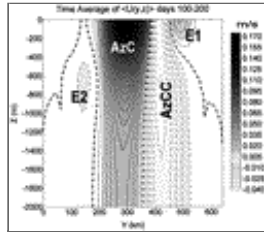
Click on thumbnail for full-sized image.

Fig. 20. Flow barotropization through geostrophic turbulent cascading. The full barotropization is never achieved because there is a continuous nudging of a baroclinic basic state.



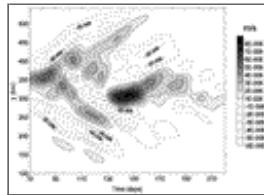
Click on thumbnail for full-sized image.

Fig. 21. Surface (a) and midwater depth ($z = 1050$ m) (b) evolution of $\bar{u}(y, z)$ field, showing AzCC in the northern flank with intensity increasing in depth. Negative values (westward flow) are shaded gray.



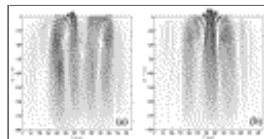
Click on thumbnail for full-sized image.

Fig. 22. Performing a time mean average for the full period comprised between days 100 and 200, according to the time mean operator: $\langle (\cdot) \rangle = (1/\Delta t) \int_t^{t+\Delta t} (\cdot) dt$, we get an $\langle \bar{u}(y, z) \rangle$ field, represented here. Mean AzCC is transporting about 4.5 Sv westward (for $380 \text{ km} < y < 500 \text{ km}$), while mean AzC is transporting some 13 Sv eastward (for $200 \text{ km} < y < 350 \text{ km}$), in good agreement with results of [section 2](#). Note the great similarity between [Fig. 2](#) in summer and the present model results. Even the E1 and E2 structures, both resulting from geostrophic turbulence rectification (as is the case of AzCC), are well reproduced at the right strength and depth. Solid (dashed) lines represent eastward (westward) flow.



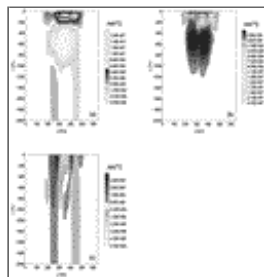
Click on thumbnail for full-sized image.

Fig. 23. Time evolution of the zonal mean vertical velocity field at $z = 370$ m. The gray shaded central upwelling band ($\bar{w} > 0$) and the nonshaded north and south downwelling zones ($\bar{w} < 0$) are showing persistent patterns relatively to the AzC axis.



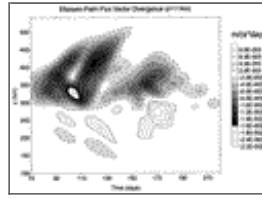
Click on thumbnail for full-sized image.

Fig. 24. The zonal mean ageostrophic field in a meridional section has a dipole structure with upwelling in the central zone and downwelling in both flanks. During the most intense instability decay period (a) (50 days time mean between days 100 and 150), two split cells can be observed. Toward the end of the instability cycle (b) (50 days time mean between days 150 and 200), the two cells became closer and both upwelling branches are merged together.



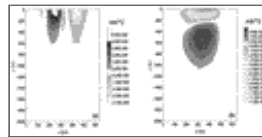
Click on thumbnail for full-sized image.

Fig. 25. Meridional pattern at day 110 of the two rhs dominant terms of (37), (a) $f\mathbf{v}_{ag}^*$ and (b) $(1/\rho_0)\nabla \cdot \mathbf{F}$. Their addition (c) shows the relative contribution for the jet acceleration/deceleration. Isocontour step is $5 \times 10^{-9} \text{ m s}^{-2}$. Dashed line are negative values and solid are positive.



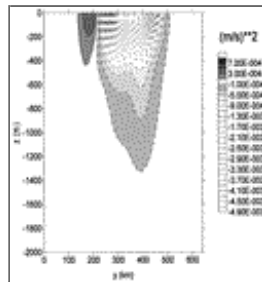
Click on thumbnail for full-sized image.

Fig. 26. The Eliassen–Palm flux vector divergence deceleration at $z = 114 \text{ m}$ is biased toward the northern flank of AzC (negative values), promoting surface AzCC during all phases of model run. Solid (dashed) lines represent eastward acceleration (deceleration). Units are $(\text{m s}^{-1} \text{ day}^{-1})$.



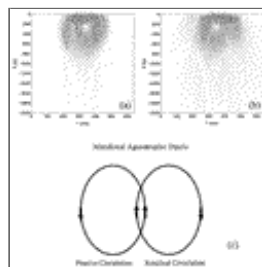
Click on thumbnail for full-sized image.

Fig. 27. Fifty-day time mean (day 100 to 150) of the two dominant terms of the Eliassen–Palm vector (43). (a) $-\partial\overline{v'u'}/\partial y$ and (b) is $[(f + \xi)/\rho_z] \partial\overline{v'\rho'}/\partial z$. The meridional divergence of $\overline{u'\mathbf{v}'}$ is causing the northward bias of $\nabla \cdot \mathbf{F} < 0$. Isocontour step is $5 \times 10^{-9} \text{ m s}^{-2}$. Dashed lines are negative values and solid are positive.




Click on thumbnail for full-sized image.

Fig. 28. Fifty-day time mean of $\overline{u'\mathbf{v}'}$ correlation (day 100 to 150). Isocontour step is $10^{-4} \text{ m}^2 \text{ s}^{-2}$. Dashed lines are negative values and solid are positive.



Click on thumbnail for full-sized image.

Fig. 29. Time mean cells of passive, $(\mathbf{v}_{ag}^0, \overline{w}^0)$ case (a) and residual, $(\mathbf{v}_{ag}^*, \overline{w}^*)$ case (b), circulation for the period 100–150 days. Note in the sketch (c) how these circulations combine to produce the ageostrophic meridional dipole (see also Fig. 24 .

Corresponding author address: Dr. Mario L. Alves, Department of Oceanography and Fisheries, Azores University, P-9900 Horta Azores, Portugal.

E-mail: mario@dop.uac.pt

top ▲



© 2008 American Meteorological Society [Privacy Policy and Disclaimer](#)
Headquarters: 45 Beacon Street Boston, MA 02108-3693
DC Office: 1120 G Street, NW, Suite 800 Washington DC, 20005-3826
amsinfo@ametsoc.org Phone: 617-227-2425 Fax: 617-742-8718
[Allen Press, Inc.](#) assists in the online publication of *AMS* journals.